Eccentric binary black hole inspiral-merger-ringdown gravitational waveform model from numerical relativity and post-Newtonian theory

Ian Hinder[*]

Max Planck Institute for Gravitational Physics (Albert Einstein Institute),
Am Mühlenberg 1, Potsdam 14476, Germany

Lawrence E. Kidder

Cornell Center for Astrophysics and Planetary Science, Cornell University,
Ithaca, New York 14853, USA

Harald P. Pfeiffer

Canadian Institute for Theoretical Astrophysics, University of Toronto, Toronto M5S 3H8, Canada
and Max Planck Institute for Gravitational Physics (Albert Einstein Institute),
Am Mühlenberg 1, Potsdam 14476, Germany

We present a prescription for computing gravitational waveforms for the inspiral, merger and ringdown of nonspinning moderately eccentric binary black hole systems. The inspiral waveform is computed using the post-Newtonian expansion and the merger waveform is computed by interpolating a small number of quasicircular NR waveforms. The use of circular merger waveforms is possible because binaries with moderate eccentricity circularize in the last few cycles before the merger, which we demonstrate up to mass ratio $q = m_1/m_2 = 3$. The complete model is calibrated to 23 numerical relativity (NR) simulations starting ≈ 20 cycles before the merger with eccentricities $e_{\mathrm{ref}} \leq 0.1$ and mass ratios $q \leq 3$, where e_{ref} is the eccentricity ≈ 7 cycles before the merger. The NR waveforms are long enough that they start below 30 Hz (10 Hz) for BBH systems with total mass $M \geq 80\ M_\odot$ ($230\ M_\odot$). We find that, for the sensitivity of advanced LIGO at the time of its first observing run, the eccentric model has a faithfulness with NR of over 97% for systems with total mass $M \geq 85 M_\odot$ across the parameter space ($e_{\mathrm{ref}} \leq 0.1$, $q \leq 3$). For systems with total mass $M \geq 70 M_\odot$, the faithfulness is over 97% for $e_{\mathrm{ref}} \lesssim 0.05$ and $q \leq 3$. The NR waveforms and the *Mathematica* code for the model are publicly available.

I. INTRODUCTION

In 2015, LIGO detected the gravitational wave (GW) event GW150914 corresponding to the merger of a binary black hole (BBH) system [1]. Subsequently, further events from BBH mergers have been detected [2,3]. The parameters of the binaries were inferred from the measured data using waveform models calibrated to numerical relativity (NR) simulations [4–6] under the very reasonable assumption that the orbit of the binary was quasicircular [7]. This is expected because binary eccentricity decays quickly under the emission of gravitational radiation [8].

Whilst there is no known mechanism by which a BBH system could retain a non-negligible eccentricity in the last ~4 orbits before merger that LIGO was able to see for the high mass event GW150914, we would like to confirm this astrophysical prediction by comparing the data to general relativistic waveforms including eccentricity. Further, several scenarios have been suggested in which binaries may retain non-negligible eccentricity for an extended time, e.g., [9–19], including some where the binary may enter the sensitive frequency band of LIGO or LISA a large number of cycles before merger, and before this eccentricity has decayed.

Gravitational wave data analysis using the method of matched filtering requires accurate models of the waveforms in order to measure source parameters. For the inspiral of eccentric binaries, models based on the post-Newtonian (PN) approximation can be used. PN theory for binaries in eccentric orbits is very well developed [8,20–41]. For a summary, see the chapter "Eccentric Compact Binaries" in [42]. However, because the approximation assumes that the black holes are widely separated and slowly moving, PN can only model the inspiral waveform.

[*]ian.hinder@aei.mpg.de

044015-1

Near the merger, the waveform can only be determined using full numerical solutions of the Einstein equations. Numerical relativity results for eccentric BBH systems[1] were first presented in [43,44]. In [44], it was found that the initial eccentricity in equal-mass eccentric binary waveforms becomes irrelevant a few cycles before the merger, provided that the initial eccentricity is not too high. At this point, to a good approximation, the binary circularizes leaving the same merger waveform and a black hole of the same final mass and spin as if the inspiral had been circular.

The first comparison between eccentric PN waveforms and NR was performed in [45], and agreement was found between 21 and 11 GW cycles before merger. Comparisons at later times were compromised by inaccuracy in the NR simulations. In [46,47], the evolution of eccentricity in NR simulations was compared with Newtonian and PN predictions and shown to be broadly consistent.

While it is possible to perform NR simulations of BBH mergers for a small number of configurations, each simulation takes several weeks to run, and is too computationally expensive to use for GW parameter estimation, where typically millions of waveforms with different parameters are generated and compared to the data. Further, the length of NR simulations is generally limited to tens of orbits, also due to computational expense. Therefore, computationally inexpensive waveform models are required, which reproduce the NR waveforms to a sufficient accuracy, and which can produce waveforms with the large numbers of orbits which may be visible to a gravitational wave detector.

The first eccentric waveform model incorporating inspiral, merger and ringdown (IMR) was presented in [48]. The inspiral is based on PN, using an improved version of the "x-model" [45], and the merger is modeled by the non-eccentric *Implicit Rotating Source* model of [49] assuming that eccentricity will be negligible by the time of the merger. The complete IMR model is called the "ax-model." An initial comparison with two NR waveforms showed that the model was realistic. Recently, two different models for eccentric binary inspiral-merger-ringdown waveforms for nonspinning BBH systems in the effective-one-body framework were proposed. In [50], the foundations of an eccentric model were presented. In [51], another model was developed, and initial comparisons were performed with three NR simulations. Finally, in [52], the model of [48] was improved by using a merger model fitted to NR simulations, as we have done here.

In this paper, we present a new set of 20 eccentric nonspinning NR simulations using the Spectral Einstein

Code (SpEC), which we have made available as part of the public catalog [53] of the Simulating eXtreme Spacetimes collaboration. The simulations have initial eccentricities $e \leq 0.2$, mass ratios $q \leq 3$ and generally start ≈ 20 cycles before the merger. The new simulations show that the circularization shortly before merger observed in [44] for equal-mass binaries extends to binaries with mass ratio $q \leq 3$. This justifies the use of circular merger waveforms in [48].

Independently of [48], we develop an eccentric IMR model based on the PN x-model [45], combined with a circular merger waveform. Our quasicircular merger waveform, which can be evaluated for any mass ratio q within the calibration region $1 \leq q \leq 4$, is obtained by interpolation between several NR waveforms with different q. For the transition region between the eccentric PN portion and the circular NR portion, we use a prescription calibrated to the new eccentric NR simulations, for which an essential ingredient is a fit of the time between the waveform reaching a given reference frequency and the peak of the waveform amplitude.

We test our model against the NR simulations, quantifying the agreement in phase, amplitude, and faithfulness (a measure of how close the waveforms are when observed by a gravitational wave detector). Since the waveforms do not agree perfectly, there is an ambiguity in the choice of PN parameters to use when comparing with a given NR waveform. We choose PN parameters such that the waveforms agree shortly before the merger, and measure the accumulation of error at preceding times. This allows us to be confident in the behavior of the model at the merger, and we expect that improvements to the PN inspiral model would extend its validity to earlier times.

The NR waveforms are available in the SXS Public Waveform Catalog [53], and a *Mathematica* package EccentricIMR implementing the full inspiral-merger-ringdown model is available as open source software at [54].

In Sec. II, we identify the main features of the eccentric PN x-model which is the basis of our IMR model. In Sec. III, we describe the NR simulations, including the code used and the eccentric configurations that we simulated. We validate the waveforms by assessing the main sources of error, and finally we show that the circularization observed in [44] extends to mass ratios $q \leq 3$. Section IV discusses the method we use to define eccentricity in NR. Section V shows how the circular merger model (CMM) is constructed by interpolating between NR waveforms. In Sec. VI, we explain how the IMR model is constructed by combining the PN inspiral with the CMM, and the calibration to NR simulations, including the time-to-merger fit, that we use for the transition. In Sec. VII, we address issues related to computing Fourier transforms of eccentric NR waveforms, required for computing the faithfulness of waveforms for gravitational wave data analysis. In Sec. VIII, we compare the IMR

---

[1]Note that determining initial conditions for a BBH system with zero eccentricity is not straightforward; as a result, all "quasicircular" BBH simulations actually have some residual eccentricity, which is typically less than 1%. This is treated as a source of error in a simulation of the desired quasicircular system.

model with the NR waveforms, analyzing both the time-domain frequencies, phases and amplitudes, as well as the Fourier-domain faithfulness relevant to gravitational wave detection and parameter estimation. Finally, Sec. IX summarizes our results, and discusses possible future improvements of our model.

Throughout, we use units in which $G = c = 1$.

II. PN INSPIRAL MODEL

In this section, we briefly review the x-model, an eccentric PN inspiral model introduced in [45] and involving a change of variables of the "n-model" presented in [30]. We begin by recalling Newtonian eccentric orbits.

Consider the relative orbit of two bodies at positions $\vec{x}_1$, $\vec{x}_2$ of masses m_1 and m_2. We restrict to the case where the bodies orbit in the xy plane, since in the nonspinning case, BBH systems will orbit in a plane due to symmetry. The separation $r = |\vec{x}_1 - \vec{x}_2|$ satisfies

$$r = a[1 - e \cos u], \qquad (1)$$

where a is the semimajor axis of the orbit, e is the eccentricity, which parametrizes the amplitude of the oscillations in r, and u is the *eccentric anomaly*, an angular variable which represents the phase of the oscillation in r. Pericenter (point of closest approach) is at $u = 0$, and $u = \pi$ corresponds to apocenter. The angular velocity of the orbit is given by

$$\dot{\phi} = \frac{n\sqrt{1 - e^2}}{[1 - e \cos u]^2}, \qquad (2)$$

where n is the *mean motion*, defined as $2\pi/P$, where P, the radial period, is the time between pericenter passages. In Newtonian dynamics, the quantities a, e, n and P are constants, which can all be expressed in terms of the energy E and angular momentum L; i.e., only two of them are independent. u can be determined by solving the Kepler equation,

$$l \equiv 2\pi(t - t_0)/P = u - e \sin u, \qquad (3)$$

a transcendental algebraic equation for u, where l is called the *mean anomaly*, and t_0 is a time corresponding to pericenter passage. l parametrizes the time elapsed since the preceding pericenter passage. Equation (3) can be solved numerically for u, for example by Newton's method, at each t. Thus we can obtain r and $\dot{\phi}$ (and hence $\dot{r}$ and ϕ) at any time t. Each orbit can be parametrized by the four independent constants a, e, $\phi(\bar{t})$ and $l(\bar{t})$ at a time $t = \bar{t}$.

The post-Newtonian *quasi-Keplerian representation* of eccentric orbits [21–28,31,55,56] is based on the above description, and utilizes the same quantities. However, the equations relating these quantities contain post-Newtonian corrections, expressed as powers of v/c. For a pedagogical introduction to the post-Newtonian Kepler

problem, see [57]. In the PN description, there are three different eccentricities, e_t, e_r and e_ϕ, related to each other by PN expressions. These are introduced to simplify certain relations. Here, we express everything in terms of $e \equiv e_t$. Relativistic eccentric orbits have the new feature of precession of the pericenter. The azimuth of the pericenter increases by $\Delta\phi$ during one radial (pericenter to pericenter) period P, so that the azimuthal coordinate ϕ increases by $2\pi + \Delta\phi$ during this time. n no longer reduces to the angular velocity $\dot{\phi}$ in the circular limit, and instead we introduce the quantity $\omega \equiv (2\pi + \Delta\phi)/P$, the average angular velocity. In the relativistic *circular* case, $\omega = \dot{\phi}$. For Newtonian orbits, further, $\omega = n$. When radiation reaction effects are neglected, ω is a constant. The choice of PN variables (for example n or ω) to use to expand the equations is arbitrary, and leads to different *approximants* once the PN series is truncated. In [45], it was found that expanding the equations in $x = (M\omega)^{2/3}$ led to better agreement between NR and PN than expanding them in n, as had been customary previously. The ω variable has the benefit of agreeing with the angular velocity used as an expansion variable in the quasicircular Taylor T4 model which has been shown to agree well with NR in the nonspinning equal-mass case [58], but we know of no deep reason why ω (equivalently x) should be better than n. We expect this good agreement to deteriorate for spinning systems or for $q \gg 1$ [59]. We parametrize the orbit in terms of the two dimensionless quantities x and e.

In the PN model, Eq. (1) remains unchanged, but Eqs. (2) and (3) are modified by PN correction terms, expanded to 3 PN order. Relativistic orbits not only differ by pericenter precession and PN correction terms, but the energy and angular momentum, which in the Newtonian case are constants, also change due to the emission of gravitational waves. In the *adiabatic approximation*, the fluxes of E and L are approximated by time averaging over a radial period P, and are used to calculate the time derivatives of x and e. These fluxes are used here to 2 PN order, as the eccentric PN code is essentially the same as that used in [45]. Extension of this code to 3 PN is left for future work.

Hence, in order to compute an orbit subject to energy and angular momentum loss, it is first necessary to solve the pair of coupled ordinary differential equations (ODEs) for $\dot{x}$ and $\dot{e}$, then compute u using the PN Kepler equation, from which l, r and ϕ are obtained.

Finally, we compute the gravitational wave using the *restricted approximation*, in which the $\ell = 2$, $m = 2$ spin weight -2 spherical harmonic mode of the waveform is given to leading (quadrupolar, Newtonian) order as

$$h^{22} = \int {}_{-2}Y_2^{2*}(\theta, \varphi)h(\theta, \varphi)d\Omega \qquad (4)$$

$$= -\frac{4M\eta e^{-2i\phi}}{R}\sqrt{\frac{\pi}{5}}\left(\frac{M}{r} + (\dot{\phi}r + i\dot{r})^2\right), \qquad (5)$$

$$h^{2-2} = h^{22*} \qquad (6)$$

(see Sec. II.A of [45] for a discussion of the origin of these expressions). Here, $_{-2}Y_2^2(\theta, \varphi) = \frac{1}{2}e^{2i\varphi}\sqrt{5/\pi}\cos^4(\theta/2)$, and θ and φ are the spherical polar angles of the observer. The $\ell = 2$, $m = \pm 2$ modes dominate for small e (see Sec. III C for a discussion of the relative strength of the subdominant modes).

For the purpose of this work, we consider the x-model as a black box, completely defined in [45], that produces $h^{22}(t)$ for a given (x_0, e_0, l_0, ϕ_0). The model is expected to be a good approximation of the relativistic dynamics when the separation is large and the velocity is small, and will break down close to the merger.

III. NR SIMULATIONS

A. NR methods

SPEC [60–63] is a pseudospectral code capable of efficiently solving many types of elliptic and hyperbolic differential equations, with the primary goal of modeling compact-object binaries. For smooth problems, spectral methods are exponentially convergent and high accuracy can be achieved even for long simulations. SPEC evolves the first order formulation [64] of the generalized harmonic formulation of Einstein's equations [65,66]. The damped harmonic gauge [67] is used to provide stable coordinate conditions. Singularities inside BHs are dynamically excised from the computational domain using feedback control systems [68,69] and initial conditions of low orbital eccentricity are obtained by an iterative evolution procedure [70]. SPEC uses h-p adaptivity[2] to dynamically control numerical truncation error and to increase computational efficiency [71]. Waveforms are extracted using the Regge-Wheeler-Zerilli formalism on a series of coordinate spherical shells and extrapolated to null infinity using polynomial expansions in powers of the areal radius [72].

B. Configurations

We aim to simulate BBH configurations with a given initial frequency parameter x, eccentricity e and mean anomaly l (see Sec. II). We use the PN approximation to translate these quantities into the initial data parameters needed by SPEC, namely the orbital angular velocity $\dot{\phi}$, the separation of the horizon centroids r, and the radial velocity $\dot{r}$. This specification of initial data parameters is only an approximation, because the PN and NR quantities are expressed in different coordinate systems, and the NR initial data contains nonastrophysical *junk radiation* which perturbs the parameters of the binary away from those given in the initial data. Nevertheless, we find that this

---

[2]h-p adaptivity refers to varying both the size, h, of the elements and the order, p, of the polynomials in each element.

prescription gives waveforms which agree to a good approximation with the PN (x, e, l). These initial data parameters are not used at any point in the subsequent analysis; all quantities are measured from the waveforms, so any discrepancy is not important.

We perform new simulations for 20 eccentric nonspinning configurations using the SPEC code. We also use three existing quasicircular nonspinning configurations already available in the SXS Public Waveform Catalog [6]. The parameters of these configurations are given in Table I. In order to assess the numerical truncation error, each configuration is run at multiple resolutions. The error analysis is presented in Sec. III D. For each of the cases 1–23, Table I gives the SXS catalog identification number, the mass ratio $q = m_1/m_2$, the orbital frequency parameter x_0 measured after the junk radiation portion of the waveform, the eccentricity e_{comm} and mean anomaly l_{comm} measured at a frequency $x_{\text{comm}} = 0.075$, the time of the peak of the amplitude of the dominant mode of the gravitational wave strain $|h_{22}|$, and the number of orbits simulated. The junk radiation portion of the waveform is considered to be the first 500 M. x, e and l are measured entirely from the waveforms by fitting to PN as described in Sec. IV. x_{comm} was chosen as the lowest frequency common to all the waveforms, and for most simulations, corresponds to a time close to the start of the simulation.

Figure 1 shows the distribution of eccentricities and mean anomalies in the parameter space. The configurations span mass ratios $q \le 3$, eccentricities $0 \le e_{\text{comm}} \le 0.2$, and mean anomalies $-\pi < l_{\text{comm}} \le \pi$. Most of the eccentric configurations start at an average orbital frequency parameter of $x \sim 0.07$ and evolve for between 11 and 15 orbits before merging.

C. Effects of eccentricity in waveforms

Figure 2 shows an example of one of the eccentric waveforms, case 9, with $e_{\text{comm}} = 0.189$. The usual oscillations in the strain (top panel) at twice the orbital frequency are modulated by an oscillating envelope with a frequency lower than the orbital frequency, corresponding to precession of the pericenter. These modulations due to eccentricity persist at least up to ~ 3 cycles before the merger. The instantaneous gravitational wave frequency (bottom panel) also shows oscillations due to eccentricity, where in the quasicircular case, the frequency would vary monotonically. The period of the oscillations in the amplitude and instantaneous frequency corresponds to the radial orbital period P, and the amplitude of the oscillations is related to the eccentricity e. The phase of the oscillations is associated with the *mean anomaly*, l. See Sec. II for the definitions of these quantities.

Our PN model contains only the dominant $\ell = 2$, $m = \pm 2$ spherical harmonic modes. We find that eccentricity introduces a modulation in the ratio between the subdominant and dominant modes at the percent level for

TABLE I. NR simulations used in this work. The columns give the case number, the SXS catalog number, the mass ratio $q = m_1/m_2$, where m_1 and m_2 are the masses of the black holes, the initial average orbital frequency parameter x_0, the eccentricity e_{comm} and mean anomaly l_{comm} measured at a frequency $x_{\mathrm{comm}} = 0.075$ common to all waveforms, the time since the start of the usable waveform at which $|h_{22}|$ reaches its peak, and the number of orbits.

Case	Simulation	q	x_0	e_{comm}	l_{comm}	t_{peak}	N_{orbs}
1	SXS:BBH:0180	1	0.0540	0.000	0.667	8720.2	26.7
2	SXS:BBH:1355	1	0.0718	0.053	−2.788	2551.6	11.9
3	SXS:BBH:1356	1	0.0582	0.069	0.963	6000.9	20.8
4	SXS:BBH:1357	1	0.0689	0.097	1.371	2888.9	12.8
5	SXS:BBH:1358	1	0.0703	0.099	−1.742	2655.8	12.1
6	SXS:BBH:1359	1	0.0711	0.100	2.743	2530.4	11.7
7	SXS:BBH:1360	1	0.0710	0.142	2.178	2372.5	11.1
8	SXS:BBH:1361	1	0.0712	0.144	1.550	2325.3	10.9
9	SXS:BBH:1362	1	0.0709	0.189	1.042	2147.0	10.2
10	SXS:BBH:1363	1	0.0710	0.192	0.732	2108.5	10.1
11	SXS:BBH:0184	2	0.0710	0.000	−0.604	3014.6	13.7
12	SXS:BBH:1364	2	0.0697	0.044	2.144	3200.3	14.2
13	SXS:BBH:1365	2	0.0696	0.060	1.938	3180.7	14.1
14	SXS:BBH:1366	2	0.0695	0.095	1.013	3073.2	13.6
15	SXS:BBH:1367	2	0.0702	0.096	−0.709	2955.2	13.3
16	SXS:BBH:1368	2	0.0708	0.097	−1.963	2850.0	13.0
17	SXS:BBH:1369	2	0.0692	0.185	−1.465	2616.4	11.9
18	SXS:BBH:1370	2	0.0709	0.185	1.778	2376.6	11.1
19	SXS:BBH:0183	3	0.0745	0.000	1.818	2811.9	13.5
20	SXS:BBH:1371	3	0.0696	0.055	−2.285	3707.4	16.2
21	SXS:BBH:1372	3	0.0695	0.092	2.998	3564.5	15.6
22	SXS:BBH:1373	3	0.0700	0.093	1.677	3451.4	15.3
23	SXS:BBH:1374	3	0.0694	0.180	−0.265	3014.6	13.5

the eccentricities we have simulated. This suggests that subdominant modes are probably no more important for these eccentricities than they are in the quasicircular case. Modeling these modes would likely be essential for much higher eccentricities.

D. Accuracy of the NR waveforms

We have verified that the NR waveforms are not dominated by numerical truncation error due to finite resolution of the simulations. The waveform phase error accumulated up to the peak of $|h_{22}|$, estimated as the difference between the highest two resolutions (see Sec. 5.2 of [73] for a discussion of how numerical errors are estimated for SPEC BBH waveforms) is less than 0.2 radians. The amplitude error during the inspiral, computed as a function of phase, is typically below 1%, but in a small number of cases is as large as 5%. The unfaithfulness (using the *aLIGO O1* detector configuration; see Sec. VII A) between the NR waveforms at different resolutions is $1 - F < 7 \times 10^{-4}$ in all cases. Some configurations, for example those for higher mass ratios, were run with higher resolution in order to attain this accuracy.

E. Circularization

In [44], it was shown that when nonspinning equal-mass black holes merge, the mass and spin of the resulting black hole were independent (within numerical error) of the eccentricity of the binary for initial eccentricities $e \leq 0.4$ (measured when the radial period $P \sim 387M$). Further, the gravitational wave frequency from binaries with different initial eccentricities was shown to be visually indistinguishable for $t > t_{\mathrm{peak}} - 50M$ (Fig. 3 of [44]). This provides evidence that the binary circularizes within $\sim 50M$ of the merger.

Here, we study this circularization for *unequal* mass systems with mass ratios up to $q = 3$. Figure 3 shows the amplitude and frequency of the gravitational wave for several eccentricities with mass ratio $q = 3$. We clearly see the effect of eccentricity as low frequency oscillations in both the frequency and amplitude of the waveform for $t < t_{\mathrm{peak}} - 30M$ (the very high frequency oscillations visible in case 23 are due to unresolved numerical truncation error). However, for $t > t_{\mathrm{peak}} - 30M$, the waveforms are visually indistinguishable. The lower panels of Fig. 3 show the relative difference between each eccentric configuration and the circular case. We see that for $t > t_{\mathrm{peak}} - 30M$, the waveform amplitude and frequency differ by only 4% for all the different eccentricities at fixed mass ratio q. For $q = 1$ and $q = 2$, we find the same behavior; irrespective of eccentricity (up to $e_{\mathrm{comm}} \lesssim 0.2$) and mean anomaly, all simulations at the same mass ratio q show nearly identical amplitude and frequency for $t > t_{\mathrm{peak}} - 30M$.
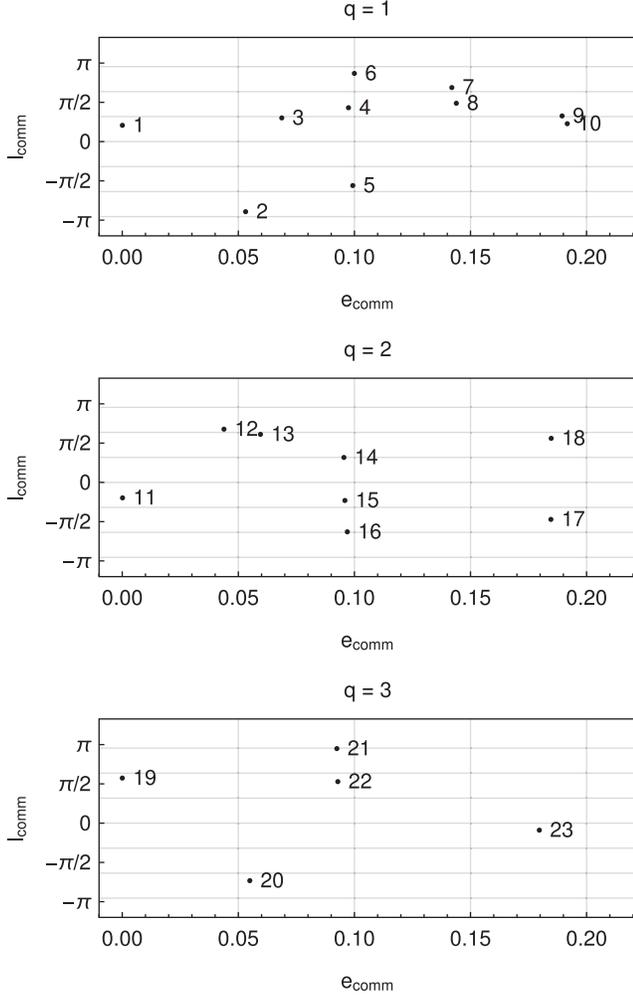
FIG. 1. The NR configurations plotted as a function of eccentricity e_{comm} and mean anomaly l_{comm} at the common frequency $x_{\text{comm}} = 0.075$ for different mass ratios q.

We interpret this to mean that the binary has circularized by $30M$ before the merger, to an accuracy of 4%. Hence, when modeling the waveform from eccentric binaries, there may be no need to use an eccentric model for the merger portion, as using a circular model instead may introduce a negligible effect on observables such as the waveform. Figure 3 justifies the use of circular merger waveforms in [48].

IV. MEASURING ECCENTRICITY

Given an eccentric waveform model, we may wish to use it to measure the parameters of a GW signal. This amounts to determining $(M, q, x(t_{\text{ref}}), e(t_{\text{ref}}), l(t_{\text{ref}}), \phi(t_{\text{ref}}); t_{\text{ref}})$ at some reference time t_{ref}. Since there is a freedom to choose t_{ref}, we quote the parameters at a fixed value of x_{ref}. For example, in Table I, we use $x_{\text{ref}} = x_{\text{comm}} = 0.075$.

In simplified terms, the parameters of a GW source are measured by comparing the measured GW strain data to the model, and determining the model parameters which best
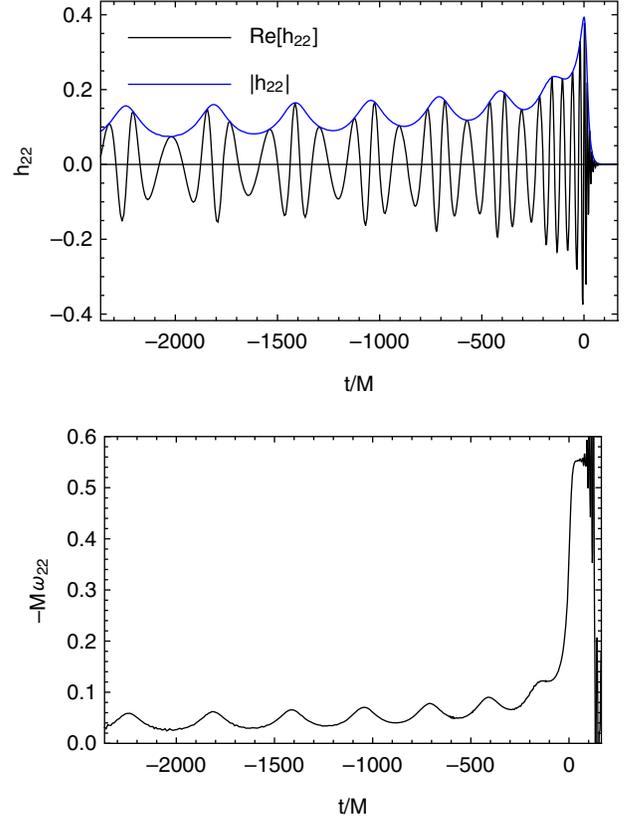
FIG. 2. An NR waveform with eccentricity $e_{\text{comm}} = 0.189$ (Case 9). The top panel shows the real part and amplitude of the dominant $\ell = 2$, $m = 2$ spherical harmonic mode of the strain, and the bottom panel shows the frequency of this mode, computed as $\omega_{22} = \frac{d}{dt} \arg h_{22}$. The oscillations in $|h_{22}|$ and ω_{22} are characteristic features of eccentricity.

reproduce the data. Note that the measured parameters are therefore PN parameters. There are plausible quasilocal GR definitions for black hole masses and spins, and we can therefore ask what *bias* is introduced in these measured parameters by using an approximate PN-based model instead of a true GR (or NR) waveform. We can determine this by fitting the PN model to an NR waveform of known masses and spins, and measuring the difference in the measured parameters.

However, in the eccentric case, the situation is complicated by the fact that there is no clear general relativistic definition of eccentricity with which to label an NR waveform (see [46,74] for various possible definitions). Our approach is to define e and l of the NR system as the PN values for which the agreement between the instantaneous NR and PN waveform frequency, $\omega_{22} = (d/dt) \arg(h_{22})$, is maximized over a single radial period centered on a reference time at which $x = x_{\text{ref}}$. This is possible because we find that the PN model we are using, with 3 PN conservative dynamics, agrees very well with NR over one radial period, as shown in [45]. The dominant error in our model is the 2 PN adiabatic evolution of x and e on timescales longer than one radial period. If the
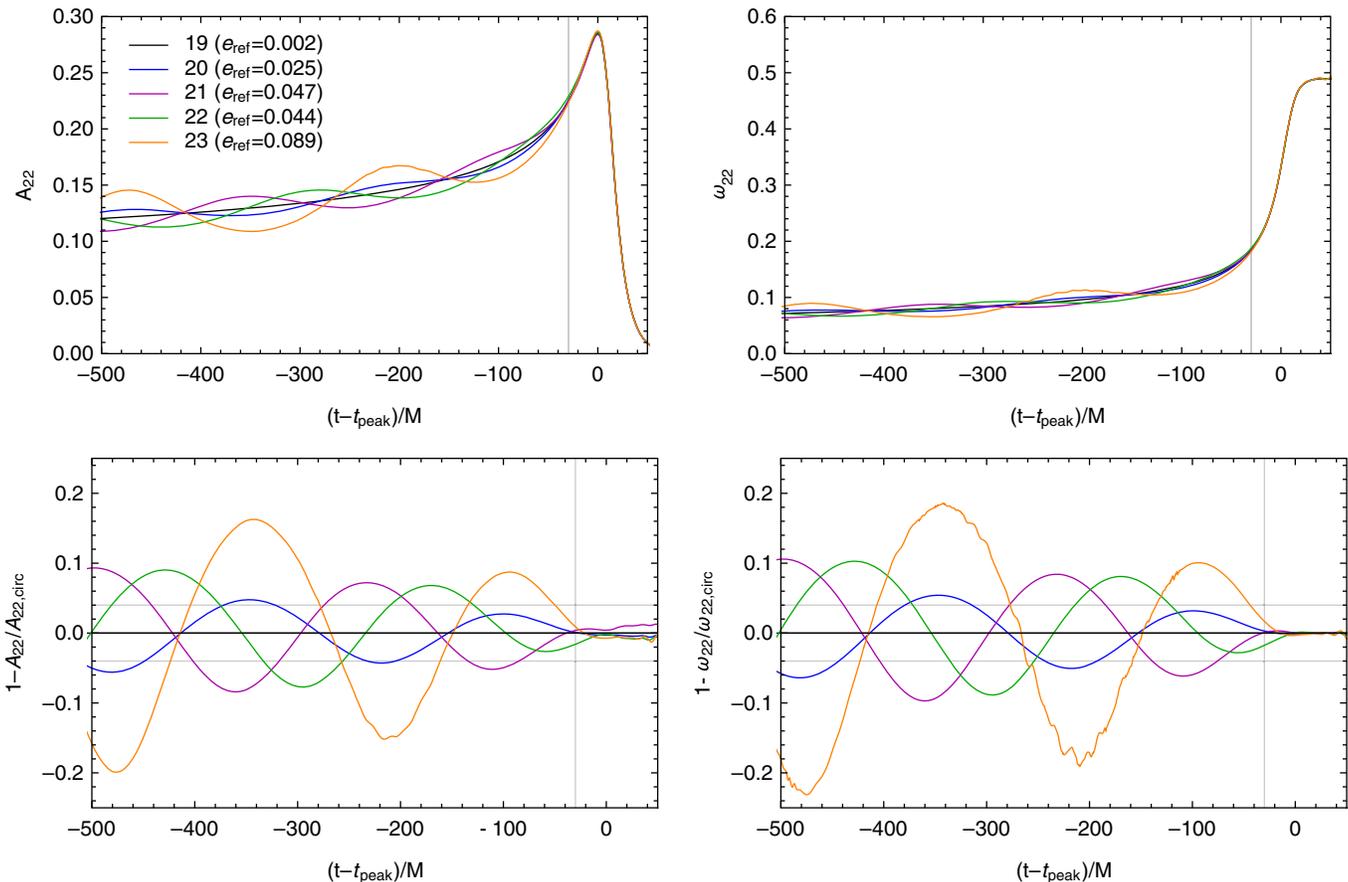
FIG. 3. Circularization of $q = 3$ nonspinning binary black hole waveforms. Shown in the upper panels are the amplitude, A, and frequency, ω_{22}, of the $l = 2$, $m = \pm 2$ mode of the gravitational wave strain. The lower panels show the fractional deviations from the noneccentric results $A_{22,\text{circ}}$ and $\omega_{22,\text{circ}}$. The gray horizontal lines in the lower panels indicate $\pm 4\%$, and the vertical lines indicate $t = t_{\text{peak}} - 30M$.

agreement over one radial period were not good, then it would be problematic to use PN to define the eccentricity of an NR waveform.

We fit the PN model to the NR data as follows. First, we choose a time window $[t_1, t_2]$ in which to fit the eccentric
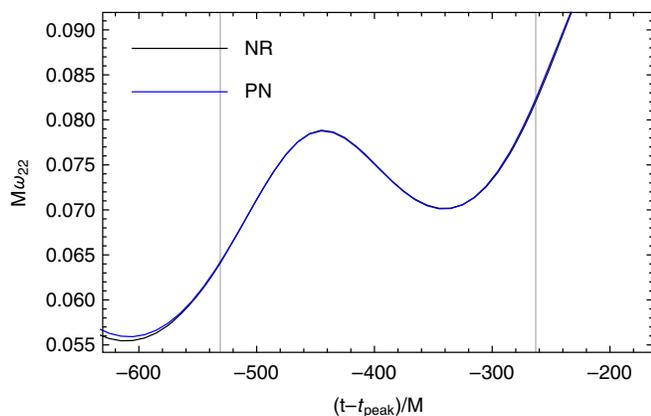
FIG. 4. PN fit to NR frequency to measure eccentric parameters at $x = 0.11$ shortly before merger. The vertical lines indicate the interval in which the fit was performed.

PN model. We then perform a least squares fit of $\omega_{22}^{\text{PN}}(x, e, l)$ to ω_{22}^{NR} to determine (x, e, l). We then perform an additional fit of $\phi_{22}^{\text{PN}}(x, e, l, \phi)$ to ϕ_{22}^{NR} to determine ϕ. This is the same procedure used in [45].

This fitting can be performed over any time interval, and gives the best-fitting PN parameters over that one interval. Since the NR and PN waveforms are not the same, the measured parameters and the resulting waveform will depend on the choice of fitting interval.

In Sec. VIII, we will compare the eccentric IMR model to the NR waveforms. For this purpose, we choose to fit the PN model to the NR waveform at $x = 0.11$, which typically occurs ≈ 7 cycles before the merger. The time interval used for fitting is centered on this point with total width equal to the radial period P. Note that the choice of fitting window therefore depends on x and P from the fit. We use an iterative process, starting from an initial guess for the fitting window location and width, and update the guess based on the result of the fit. We use the parameters measured at this point to label the waveform. The rms fit error in each case is $\leq 1\%$, indicating that the PN model accurately describes the

waveform on a timescale of one radial period close to the merger.

For the configuration with $q = 1$ and $e_{comm} = 0.1$ (case 6), the comparison between ω^{NR} and ω^{PN} for the $\ell = 2$, $m = 2$ mode, fitted across one radial period at $x = 0.11$, is shown in Fig. 4. The vertical lines indicate the interval in which the fit was performed. Note that this procedure for choosing the PN parameters corresponding to an NR waveform is not unique. For example, in [45], a longer fitting interval near the start of the NR waveform was chosen. Our motivation in this work is to accurately model the merger, so we choose to make the NR and PN waveforms agree close to the merger, and then evaluate the growth in error at earlier times.

V. CIRCULAR MERGER MODEL

As shown in Sec. III E, the eccentric NR waveforms circularize before the merger, suggesting that it should be possible for an eccentric waveform model to incorporate a circular model for the merger. Any circular waveform model should be sufficient; for example, the implicit-rotating-source (IRS) model [49] used in [48], effective-one-body models such as SEOBNRv4 [75], the so-called *phenomenological* models, for example IMRPhenomD [5,76], or surrogate models [77] formed by interpolating NR waveforms. As shown in Fig. 4 of [48], the IRS model does not match the NR data perfectly, and the EOB and surrogate models introduce additional complications to our model which are not necessary for modeling the straight-forward waveform from a nonspinning BBH merger. Hence, we created a very simple model for the merger waveform by performing an interpolation in q of a small number of noneccentric nonspinning NR waveforms in the neighborhood of the merger. The resulting circular merger model (CMM) can be evaluated for $1 \leq q \leq 4$ and arbitrary ϕ_0, corresponding to the initial phase of the waveform. This model agrees well with noneccentric NR waveforms. Note that there is no attempt to ensure validity for $q > 4$, and it will very likely break down for these mass ratios, though extension of the method to higher mass ratios should present no difficulties.

To construct the CMM, we take three nonspinning *input* waveforms from the SXS waveform catalog [6] with mass ratios 1, 2 and 4 (SXS:BBH:0180, SXS:BBH:0184 and SXS:BBH:0182, respectively), and apply a time shift such that the peak of $|h_{22}|$ is at $t = 0$. We thus obtain $h^{NR}(t, q_i)$ for $i = 1, 2, 3$. For each waveform, we then compute the amplitude $A^{NR}(t, q_i) = |h^{NR}(t, q_i)|$ and instantaneous frequency $\omega^{NR}(t, q_i) = (d/dt) \arg(h^{NR}(t, q_i))$, and interpolate them to a common uniform time grid $t \in [-500M, 80M]$ with spacing $0.4M$, resulting in 1450 sample points. At each time, we construct a second order interpolating function in q for A and ω across the mass ratios q_i. This set of 2×1450 interpolants constitutes the model.

To create a circular merger waveform at arbitrary (q, ϕ_0, t_{peak}), we evaluate these interpolants at each sample time with the desired q, integrate the resulting ω numerically to get ϕ, choosing an appropriate integration constant, then compute the strain h from A and ϕ. This constitutes the circular merger model (CMM).

To test the CMM, we use additional SXS catalog waveforms with mass ratios $q = 1.5, 2.5, 3.0, 3.3, 4$ (also used in [77]). Figure 5 shows a comparison between the CMM and each of the test waveforms. The solid lines are the NR data, and the dashed lines are the CMM. We see that in all cases, A and ω are visually indistinguishable between the NR and CMM results, except for some oscillations in ω at $t > t_{peak} + 50M$. The phase and amplitude differences between NR and the CMM are also plotted, and we see that the maximum phase error in the CMM is ~ 0.15 radians, and the maximum amplitude error is $\sim 10\%$ at late times, but only $\sim 3\%$ if the low amplitude portion at the end of the ringdown is excluded.[3]

In order to evaluate the faithfulness of the CMM with the NR waveforms, we have combined the inspiral of an NR test waveform with the merger from the CMM, blended using a transition function $\mathcal{T}$ [see Eq. (20)] in the region $t - t_{peak} \in [-100M, -80M]$. As shown in Fig. 5, the unfaithfulness in each case is $1 - F < 4 \times 10^{-4}$ using the *aLIGO O1* detector configuration (see Sec. VII A).

VI. CONSTRUCTION OF AN IMR WAVEFORM MODEL

A. Motivation and approach

We have described the eccentric PN model for the inspiral, and a circular model for the merger, and have shown that the merger from NR is essentially circular. We now define a method for combining the PN inspiral (*x*-model) with the circular merger model (CMM) based on a simple blending of the two models in a transition region. We will evaluate afterwards how well this has worked.

The starting point is the reference time, at which $x = 0.11$. We choose the parameters (x_0, e_0, l_0, ϕ_0) at this time, t_{ref}. We compute the waveform from PN for $t < t_{ref}$. We use the CMM for $t > t_{circ} \equiv t_{peak} - 30M$, since we have shown that a circular model is good after $30M$ before the peak. Note that we do not yet know the time at which the peak occurs, given the time of the reference point, $\Delta t = t_{peak} - t_{ref}$.

If the PN waveform agreed well with the NR waveform for $t < t_{circ}$, the model would now be complete, because we could match the circular waveform frequency and phase to the PN frequency and phase at $t = t_{circ}$. Unfortunately, the PN waveform cannot be extended reliably up to t_{circ}, and it

---

[3]In fact, the test waveforms have higher numerical truncation error than the input waveforms, and this error is comparable to the differences between the CMM and the test waveforms.
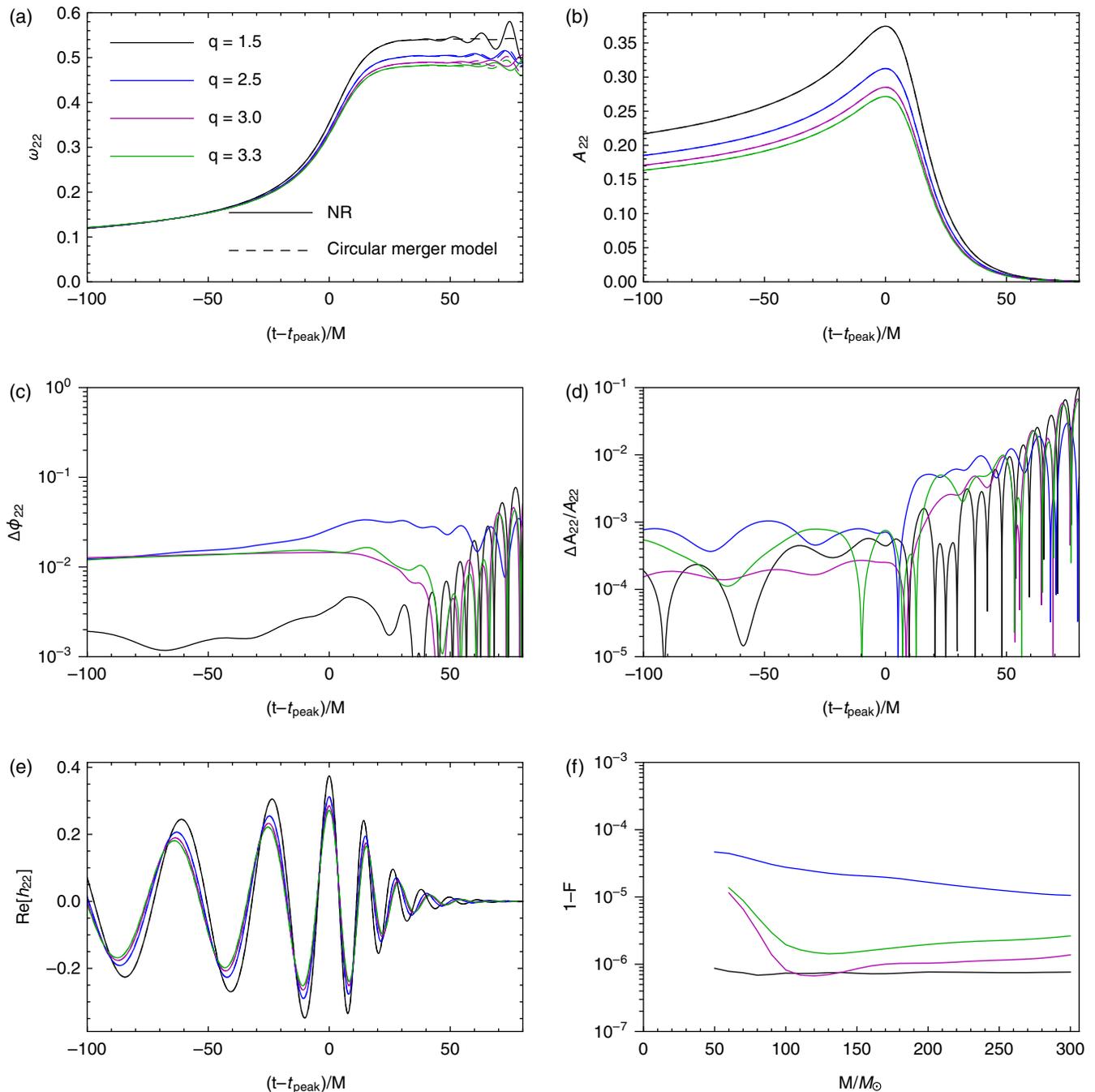
FIG. 5.   Tests of the circular merger model (CMM) for NR waveforms which were not used to construct it. Plotted in (a) and (b) are the GW frequency and amplitude from NR simulations (solid curves) and the CMM (dashed curves). We see good agreement. In (c) and (d) are plotted the phase and relative amplitude differences between NR and the CMM. (e) shows the real part of the $\ell = 2$, $m = 2$ mode of the gravitational wave strain, and (f) shows the unfaithfulness between NR and the CMM using the *aLIGO O1* detector configuration (see Sec. VII A).

disagrees with the circular NR waveform between $t_{\rm ref}$ and $t_{\rm circ}$, so this procedure would result in a merger waveform with a noticeable error in the time and phase of the peak. This is not surprising, because the PN approximation is not expected to be good so close to the merger.

Instead, we adopt a simple model for the time to merger Δt and fit it to the NR simulations. This model works very well, and essentially guarantees that the final IMR model will have the waveform peak at the correct time, to within the errors in Δt. Once we have Δt, we blend the eccentric PN waveform with the circular NR interpolated model between $t_{\rm ref}$ and $t_{\rm circ}$. There will be a discrepancy between the model and NR in this region, and the validity of this model will be assessed in Sec. VIII.

B. Time to merger

We now determine $\Delta t = t_{\text{peak}} - t_{\text{ref}}$ given the parameters at t_{ref}. The most general functional form would be

$$\Delta t(q, e, l) = \sum_{ijk=0}^{\infty} a_{ijk} q^i e^j \cos(kl - \alpha_{ijk}), \qquad (7)$$

where we use a Taylor expansion in q and e, and a Fourier series in l, since l is a periodic variable. In order to match the NR data, we find that we require quadratic terms in q and e, but only the first mode in l. Since there can be no variation with l when $e = 0$, we must have $a_{i01} = 0$. The resulting model for Δt is

$$\Delta t(q, e, l) = \Delta t_0 + a_1 e + a_2 e^2 + b_1 q + b_2 q^2$$
$$+ c_1 e \cos(l + c_2) + c_3 eq. \qquad (8)$$

There are eight unknown parameters, and the model is fitted to all 23 simulations. The fitted function is

$$\Delta t(q, e, l) = 391.196 + 3.13391e - 2492.95e^2$$
$$+ 2.77212q - 17.92eq + 8.11842q^2$$
$$+ 76.4944e \cos(0.626653 + l). \qquad (9)$$

Figure 6 shows Δt for each NR simulation, along with the value obtained from the fit. The fit residual is less than $\pm 1M$, and the essential functional dependence of $\Delta t(q, e, l)$ has been captured by the model. We conclude that the time of the peak can be predicted from the parameters at t_{ref} to within $\pm 1M$.

C. Combining all the ingredients

Given the eccentric parameters (x_0, e_0, l_0, ϕ_0) at t_{ref}, we now construct a full IMR waveform. The eccentric PN
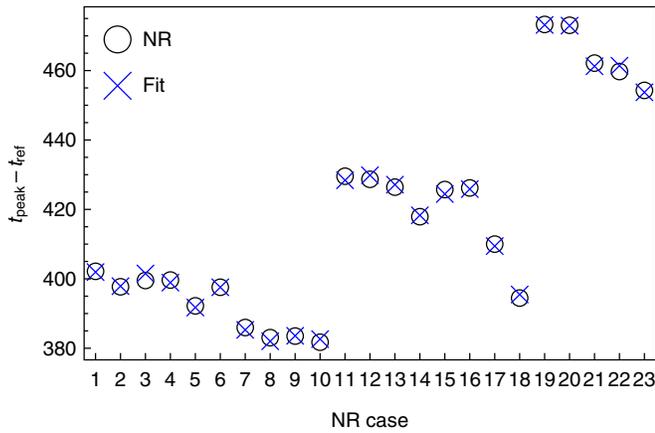
FIG. 6. Agreement of the time-to-merger model with NR. The time between the reference point and the peak of $|h_{22}|$ is shown as a circle for each NR simulation, and a cross for the fitted model from Eq. (9).

waveform is $h^{\text{PN}}(t)$, such that its parameters at $t = t_{\text{ref}}$ match the desired model parameters. The circular merger waveform is $h_{\text{circ}}(t)$, such that the peak occurs at $t = 0$. The waveform is decomposed into amplitude, A, and frequency, ω, as $h = A e^{i\phi}$, and $\dot{\phi} = \omega$. The IMR waveform is given by

$$t_{\text{peak}} = t_{\text{ref}} + \Delta t \qquad (10)$$

$$t_{\text{circ}} = t_{\text{peak}} - 30M \qquad (11)$$

$$t_{\text{blend}} = t|_{x=x_{\text{blend}}} \qquad (12)$$

$$\alpha(t) = \mathcal{T}(t; t_{\text{blend}}, t_{\text{circ}}) \qquad (13)$$

$$A(t) = \alpha(t) A^{\text{PN}} + (1 - \alpha(t)) A^{\text{circ}}(t - t_{\text{peak}}) \qquad (14)$$

$$\omega(t) = \alpha(t) \omega^{\text{PN}} + (1 - \alpha(t)) \omega^{\text{circ}}(t - t_{\text{peak}}) \qquad (15)$$

$$\phi(t) = \int^t \omega(t') dt' \qquad (16)$$

$$h(t) = A(t) e^{i\phi(t)}. \qquad (17)$$

The start of the blending region is chosen as $x_{\text{blend}} = 0.12$, and the reference point as $x_{\text{ref}} = 0.11$. In words, we time shift the circular waveform so that its peak is in the correct place according to the time-to-merger fit of Sec. VI B, and blend the amplitude and frequency of the PN and circular waveforms using a transition function $\mathcal{T}$ [see Eq. (20)] between t_{blend} and t_{circ} to ensure a smooth transition in these quantities. The phase is then computed by integrating the frequency, leading to the final waveform.

This procedure is illustrated for case 6 in Fig. 7, which shows the amplitudes and frequencies from PN and the circular model, as well as the transition region in which they are blended. The NR waveform is shown for comparison, but no information from the NR waveform (other than the set of fit parameters at t_{ref}) is used in computing the model waveform.

We see in Fig. 7 that the IMR waveform ω agrees with PN and NR before t_{ref}, and with the CMM after t_{circ}. There is a visible discrepancy between the IMR and NR frequency between t_{ref} and t_{circ}, though this is small. The PN waveform breaks down after t_{circ}. The IMR amplitude A has a visible disagreement with the NR amplitude, presumably due to the fact that zeroth-order PN (restricted) waveform amplitudes are used in the model.

VII. FOURIER DOMAIN COMPARISONS OF WAVEFORMS

In this section, we discuss the comparison of waveforms from the point of view of gravitational wave data analysis,
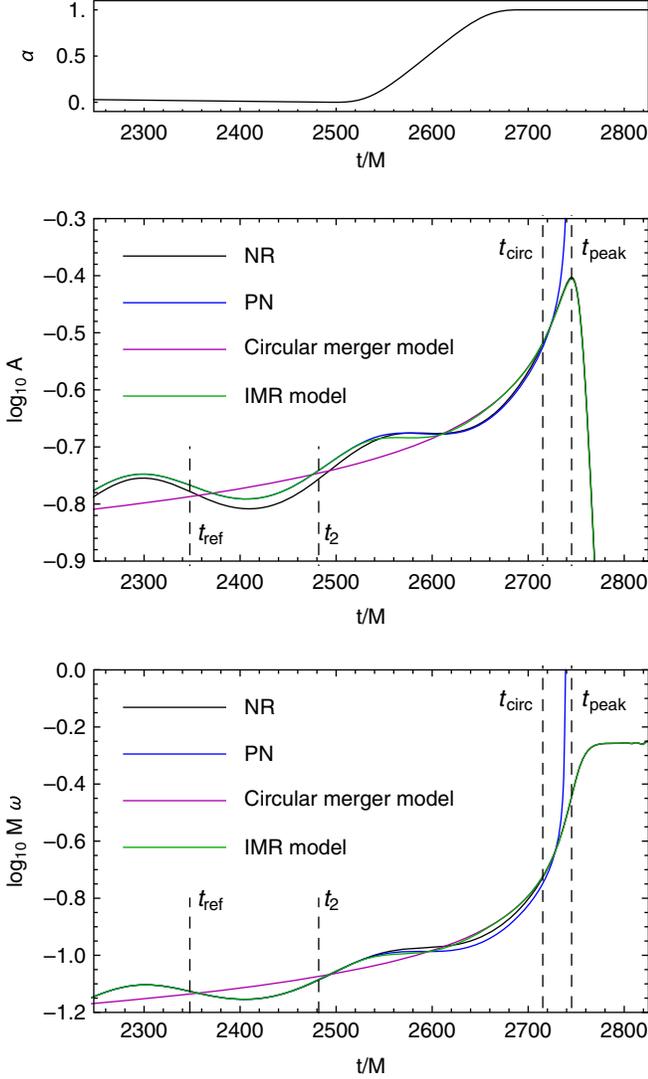
FIG. 7. Combining the different ingredients to produce the IMR waveform. The top panel shows the transition function α which is used to blend the amplitude, A, and frequency, ω, between the eccentric PN and circular NR waveforms. The middle and bottom panels show A and ω from the NR simulation, the PN model fitted to it at the reference point t_{ref}, and the circular merger model (CMM) with peak t_{peak} determined from the time-to-merger fit ΔT. The IMR model is constructed by blending the PN and CMM quantities using α. t_2 indicates the end of the fitting window.

which requires Fourier representations of the waveforms. We investigate the effect of eccentricity on the procedure used to ensure that Fourier transforms of time-domain truncated waveforms are reliable.

A. Faithfulness

The primary method for analyzing data from a gravitational wave detector for compact-binary mergers is matched filtering against a set of template waveforms in the frequency domain (for example, see [78,79] for methods used in detection, and [80] for parameter

estimation). In Sec. VIII E, we will determine how well the eccentric IMR waveform model defined in Sec. VI agrees with potential astrophysical sources. Given two waveforms $h_1(t)$ and $h_2(t)$, their noise-weighted *overlap* is defined as [81]

$$(h_1|h_2) \equiv 4\mathrm{Re} \int_{f_{\min}}^{f_{\max}} \frac{\tilde{h}_1(f)\tilde{h}_2^*(f)}{S_n(f)} df, \qquad (18)$$

where $\tilde{h}_{1,2}(f)$ are the Fourier transforms of the waveforms and $S_n(f)$ is the one-sided power spectral density (PSD) of the detector noise.

We examine two Advanced LIGO detector configurations. The first, *aLIGO O1*, is representative of the sensitivity of LIGO during its first observing run. The noise PSD [82] is the one which was used to place templates for the O1 search, as described in [78], and we restrict to a frequency range $f_{\min} = 30$ Hz, $f_{\max} = 2050$ Hz. The second configuration, *aLIGO design*, is representative of the sensitivity expected for the final design configuration of Advanced LIGO. The noise PSD is the zero-detuned-high-power variant from [83], with a frequency range $f_{\min} = 10$ Hz, $f_{\max} = 8192$ Hz.

The *faithfulness* [84] between two waveforms is then defined as the overlap between the normalized waveforms maximized over relative time and phase shifts,

$$F = \max_{\phi_c, t_c} \frac{(h_1(\phi_c, t_c)|h_2)}{\sqrt{(h_1|h_1)(h_2|h_2)}}. \qquad (19)$$

The faithfulness measures how similar the waveforms would appear to a gravitational wave detector when the data is analyzed using matched filtering.

B. Fourier transforms of eccentric NR waveforms

Computation of the faithfulness, Eq. (19), requires the Fourier transforms of the waveforms h_1 and h_2, which will correspond to the IMR model waveform and the "true" astrophysical waveform, which we take to be the NR waveform. Hence, we need to compute the Fourier transforms of these waveforms.

To estimate the continuum Fourier transform, we use a discrete Fourier transform over the available NR time interval (see, e.g., [85]). To minimize Gibbs' phenomena due to time-domain truncation, the waveform is tapered by multiplying it by a variant of the Planck taper function [86],

$$\mathcal{T}(t; t_1, t_2) = \begin{cases} 0 & \text{for } t \le t_1 \\ \left[\exp\left(\frac{t_2 - t_1}{t - t_1} + \frac{t_2 - t_1}{t - t_2}\right) + 1\right]^{-1} & \text{for } t_1 < t < t_2 \\ 1 & \text{for } t \ge t_2 \end{cases} \qquad (20)$$

at both the start and end of the waveform. Specifically,

$$h_{\ell m}(t) \rightarrow h_{\ell m}(t) \qquad (21)$$

$$\times \mathcal{T}(t; t_{\text{rel}}, t_{\text{rel}} + 250M) \qquad (22)$$

$$\times (1 - \mathcal{T}(t; t_{\text{peak}} + 60M, t_{\text{peak}} + 80M)). \qquad (23)$$

t_{rel} is the *relaxed* time, after which the effects of non-astrophysical junk radiation in the waveform can be neglected (here chosen as $500M$ from the start of the waveform), and t_{peak} is the time of the peak in $|h_{22}|$, roughly corresponding to the merger. The waveform is also resampled to a time step of $0.4M$ (higher frequency content is not important here) and padded with zeros before computing the discrete Fourier transform to ensure a sufficiently small time step in frequency space.

In the quasicircular case, $\omega_{22}(t) \approx 2\dot{\phi}$, where $\omega_{22}(t)$ is the frequency of the dominant instantaneous GW emission from the binary, and $\dot{\phi}$ is the orbital angular velocity. $\dot{\phi}$ increases monotonically on the radiation-reaction time-scale. Intuitively, $\tilde{h}(\omega)$ consists of contributions from times when $\dot{\phi} \approx \omega/2$ (an application of the stationary phase approximation; see for example [87,88]). The amplitude of the Fourier transform is $|\tilde{h}_{22}| \sim (M\omega)^{-7/6}$ to leading PN order; i.e., it decreases with increasing ω because the binary spends more time, and hence there is more total GW emission, at lower frequency than at high frequency, and the increase in the amplitude of emission per orbit at high frequency is not enough to dominate over this effect.

A quasicircular NR simulation starts with a given orbital angular velocity $\dot{\phi}_0$, and contributions to $\tilde{h}(\omega)$ for $\omega < 2\dot{\phi}_0$, which would be present in a real astrophysical waveform, are not present in the NR waveform. In other words, $\tilde{h}(\omega)$ for the time-truncated waveform is *unphysical* below a certain frequency, and its amplitude is strongly suppressed for $\omega < 2\dot{\phi}_0$. Hence, there is a peak at $\omega_{\text{peak}} \approx 2\dot{\phi}_0$ in the Fourier transform of the truncated waveform. Typically, $\tilde{h}(\omega)$ is found to be relatively free of Gibbs' phenomena and agrees with longer waveforms for $\omega > 1.2\omega_{\text{peak}}$ [89].

In the eccentric case, there is no longer a single frequency emitted at a given time, and $\omega_{22} \approx 2\dot{\phi}$ oscillates on the *orbital* timescale [see Eq. (2)], so it is not clear that the minimum frequency at which $\tilde{h}(\omega)$ is reliable can be determined using the same criterion in the eccentric case as in the circular case.

In order to assess the effect of time truncation, we have run one simulation, case 3, starting from a lower orbital frequency than the others, giving 40 cycles rather than the typical 20, and $\sim 6000M$ of evolution time, rather than the typical $2500M$.

Figure 8 shows the amplitudes of the Fourier transforms of waveforms with $e_{\text{comm}} = 0.000$ and 0.069 (case 1 and case 3). The eccentric waveform is plotted twice; once truncated in the time domain $6000M$ before merger, and once truncated $2500M$ before merger. We see that at high
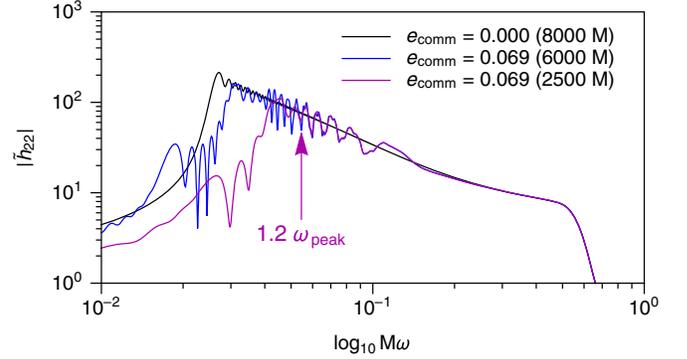
FIG. 8. Fourier transforms of circular and eccentric waveforms. The eccentric waveform has been truncated in the time domain to two different lengths. This allows us to assess the effect of time-domain truncation on the Fourier transform.

frequency ($M\omega > 2 \times 10^{-1}$), the effect of eccentricity on the waveform is negligible, indicating that the merger waveform is more or less independent of eccentricity. At intermediate frequency ($4 \times 10^{-2} < M\omega < 2 \times 10^{-1}$), we see the oscillations in $|\tilde{h}_{22}|$ for the eccentric waveforms characteristic of eccentricity. The eccentric waveform appears independent of time truncation for $M\omega \gtrsim 5 \times 10^{-2}$. The peaks in the amplitudes of $\tilde{h}$ are visible between 2×10^{-2} and $\sim 10^{-1}$, depending on the configuration, and for $\omega < \omega_{\text{peak}}$ in each case, the amplitude drops rapidly to 0 as $\omega \rightarrow 0$. In this case, it appears that $\tilde{h}(\omega)$ is independent of time truncation for $\omega > 1.2\omega_{\text{peak}}$, as in the circular case, and we assume this in the analysis that follows. This is only a preliminary check of the effect of time truncation on eccentric waveforms, and a more detailed study in the future would be beneficial.

To ensure that the integral in Eq. (18) only covers the physical part of the waveform $f > 1.2f_{\text{peak}}$, we restrict to computing the unfaithfulness for systems for which $1.2f_{\text{peak}} < f_{\text{min}}$. f_{peak} scales inversely with the total mass of the system, so it is only possible to compute the unfaithfulness for systems with total mass $M > M_{\text{min}}$, where M_{min} depends on both the length of the NR waveform, and the particular GW detector considered. If longer NR waveforms starting from lower frequency were available, the unfaithfulness could be computed for lower mass systems.

VIII. MODELING RESULTS

We have described how to generate an eccentric IMR waveform for a given e_0 and l_0. This model will now be tested by comparing the waveforms from the IMR model to NR. The parameters of the PN waveforms used in the comparison are obtained by fitting $\omega^{\text{PN}}(e_{\text{ref}}, l_{\text{ref}})$ to ω^{NR} in a one period window centered on at $x = x_{\text{ref}} = 0.11$ as described in Sec. IV. The relative residual for this fit is less than 1% in all cases.

A. Instantaneous gravitational wave frequency

Since the PN parameters of the NR waveform are determined by fitting the instantaneous GW frequency ω_{22}, this quantity is expected to agree the best between NR and the model, at least within the fitting window. Figure 9 shows ω_{22} as a function of time for three of the NR simulations. In each case, the fit window is highlighted. The top panel shows Case 53 ($q = 3$, $e_{\text{ref}} = 0$), representing the quasicircular limit of the model. We see that at the highest mass ratio studied here, ω_{22} from NR and the model agree well for the duration of the NR waveform. The middle panel shows case 6 ($q = 1$, $e_{\text{ref}} = 0.05$). For this equal-mass case with moderate eccentricity, the phase and amplitude of the oscillations in the NR ω_{22} are reproduced well by the model, though there is some dephasing seen at early times. This shows that the radiation reaction in the model does not perfectly capture the evolution of the advance of pericenter, $\Delta\phi$. The bottom panel shows case 23 ($q = 3$, $e_{\text{ref}} = 0.09$). This is the most extreme
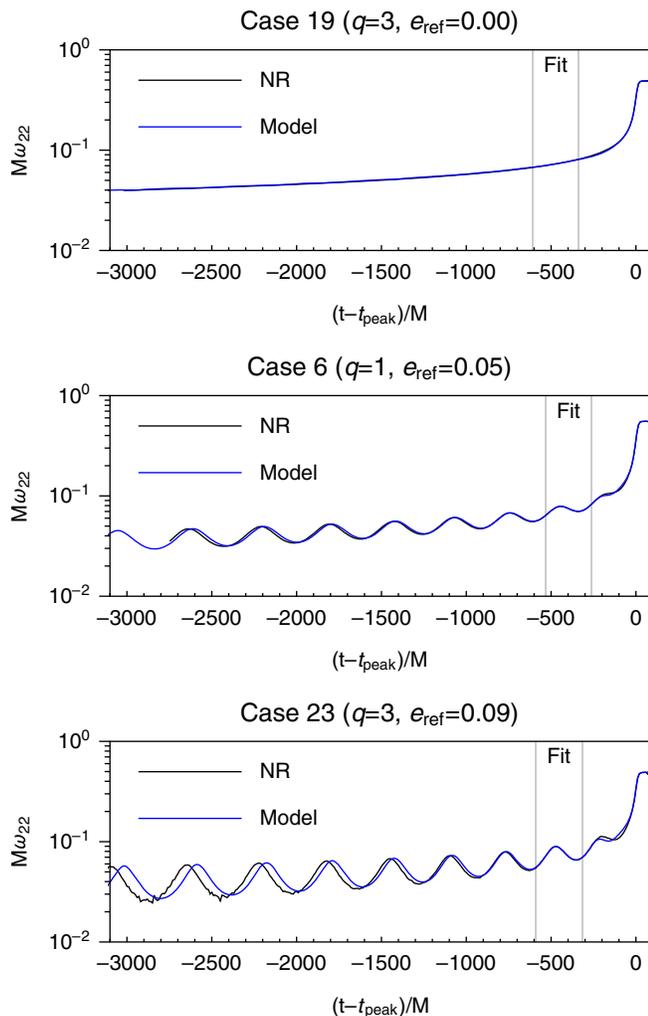
configuration studied, with the highest eccentricity and mass ratio, and shows the limitations of the model. The dephasing in ω_{22} at early times is clearly visible, as is the error between the fit window and the merger.

These three cases are examples which broadly represent the performance of the model across the whole set of NR configurations. We conclude that the model reproduces the NR ω_{22} well, but the agreement, especially at early times, becomes worse with increasing mass ratio and eccentricity.

B. Strain

Figure 10 shows the real part of the strain, $\text{Re}[h_{22}]$ from both NR and the model. The right panels highlight the merger and ringdown, and while the agreement is not perfect, the model largely agrees with NR. There is some dephasing visible at early times for the quasicircular $q = 3$ case. The equal-mass case with moderate eccentricity agrees very well with NR. As for the frequency, for the case with the highest mass ratio and eccentricity, there is noticeable dephasing at early times between the model and NR. Again, this may be improved by using 3 PN radiation reaction terms in the model.

C. Phase

Figure 11 shows the phase error in the model waveform; $\Delta\phi = \arg h_{22}^{\text{NR}} - \arg h_{22}^{\text{model}}$. For most of the waveforms, the phase error of the circular case gives a lower bound on the error of the eccentric cases. For $e_{\text{ref}} \lesssim 0.05$, the phase error oscillates between the circular value and a value a few times larger. There is no appreciable effect of eccentricity on the secular growth of the phase error for these eccentricities, suggesting that the effect of eccentricity on the error in the adiabatic evolution is negligible. For higher eccentricities, this is no longer the case, and eccentricity appears to increase the secular phase error.

We expect that adding higher order radiation reaction terms to the model, as in [48], will decrease the phase error.

Note that for the quasicircular cases 11 and 19, the eccentricity measured at $x = 0.11$ is higher than that measured at $x = 0.075$. This discrepancy, affecting the third decimal place, may be an indication of the error in the eccentricity-estimation procedure, especially close to the merger where the secular growth in ω_{22} may be confused with oscillations due to eccentricity.

D. Amplitude

Figure 12 shows the relative difference in the amplitude, $A = |h_{22}|$, between the NR and model waveforms. Note that we plot $A(\phi)$ instead of $A(t)$, so that phase and amplitude errors are decoupled. The amplitude error varies between 4% and 13%.

The IMR model incorporates 0 PN restricted waveforms; i.e., the expression for the waveform in terms of the orbital quantities, Eq. (5), is given by the quadrupole

FIG. 9. Gravitational wave frequency comparison between IMR model and NR.
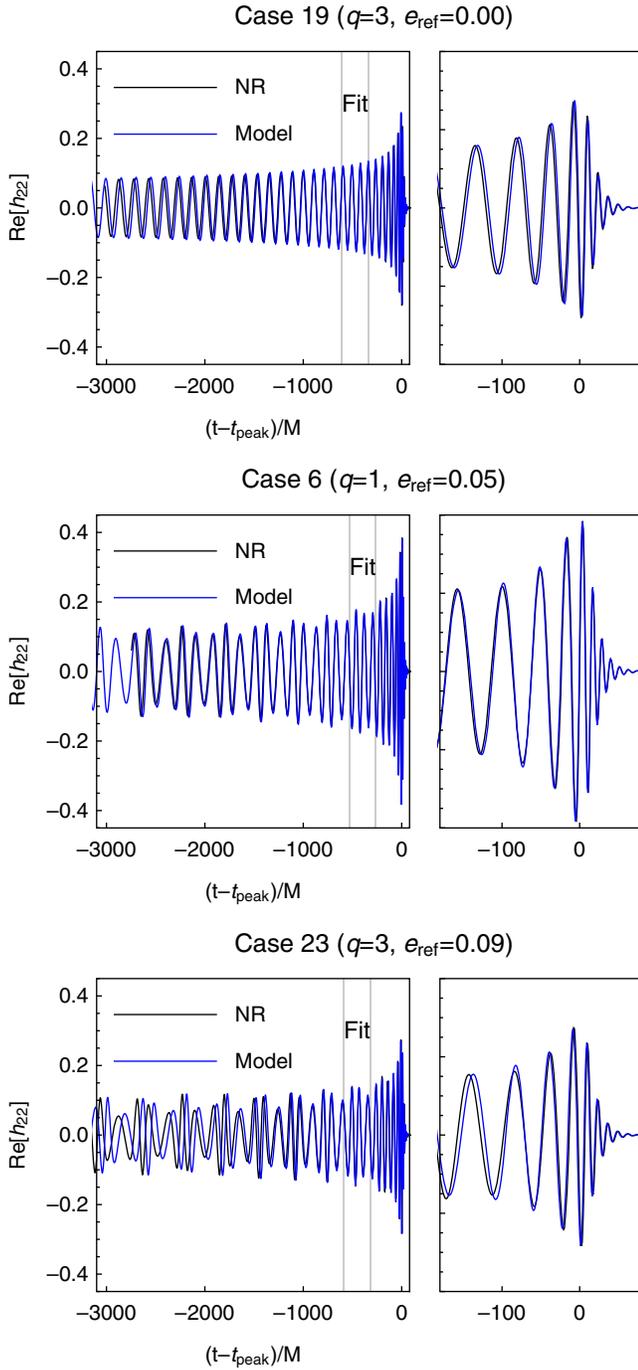
FIG. 10. Gravitational wave strain comparison between IMR model and NR. Top: quasicircular case with $q = 3$; some dephasing is visible. Middle: an eccentric equal-mass case, which shows excellent agreement. Bottom: $q = 3$ with the highest eccentricity configuration, which shows the worst agreement of all the cases.

FIG. 11. Phase difference between IMR model and NR.

formula. State-of-the-art quasicircular models use waveforms based on at least 3 PN accurate expressions in the nonspinning case. In the quasicircular case, it has been shown (e.g., in [58]) that the use of lower order waveforms primarily affects the amplitude rather than the phase, so it is

not surprising to see relatively large amplitude error here, even in cases where the phase errors are fairly small.

E. Faithfulness

Figures 13 and 14 show, for each mass ratio q, the unfaithfulness between the model and each NR waveform for the two advanced LIGO detector configurations *aLIGO O1* and *aLIGO design* (see Sec. VII A). The unfaithfulness is plotted only for the source masses for which the entire NR waveform is in the sensitive
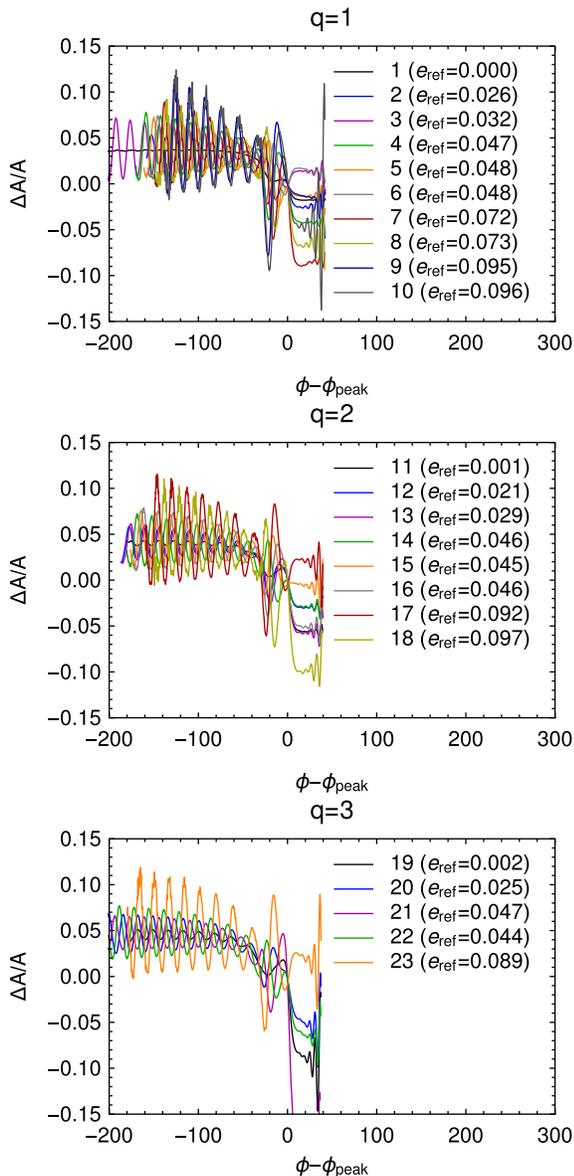
FIG. 12.   Amplitude difference between IMR model and NR.

FIG. 13.   The unfaithfulness, $1 - F$, for the *aLIGO O1* detector configuration, between the eccentric IMR model and the NR simulations, as a function of the total binary mass. Masses for which the NR waveform starts at a frequency higher than the detector's $f_{\min}$ are omitted from the plot. The horizontal line shows the 3% unfaithfulness target, and the vertical line shows $70 M_{\odot}$, roughly corresponding to the mass of GW150914.

frequency band of the detector. The unfaithfulness gets higher as either eccentricity or mass ratio increases.

For *aLIGO O1*, with a low frequency cutoff of 30 Hz, the model has an unfaithfulness of less than 3% for $q = 1$ across the entire mass range covered by the NR waveforms, or $M \geq 80 M_{\odot}$. For $q = 3$, the highest eccentricity waveforms have unfaithfulness less than 3% only for slightly higher masses, namely $M > 90 M_{\odot}$. By extrapolating the results in Fig. 13 to lower mass, it appears that the unfaithfulness of the highest eccentricity waveforms would probably exceed the 3% target for masses $\lesssim 70 M_{\odot}$.

For *aLIGO design*, with a low frequency cutoff of 10 Hz, the model has faithfulness 3% for all mass ratios and eccentricities for which the NR waveform is entirely in band, however most of the NR waveforms are too short

to compute unfaithfulness for $M \lesssim 180 M_{\odot}$. In general, for a given total mass, the unfaithfulness with *aLIGO design* is greater than with *aLIGO O1*, so it is reasonable to expect that at masses $\approx 70 M_{\odot}$, the highest eccentricity waveforms would also exceed the unfaithfulness target of 3%.

Longer NR waveforms, reaching lower frequencies (for which the entire waveform is in the sensitive band
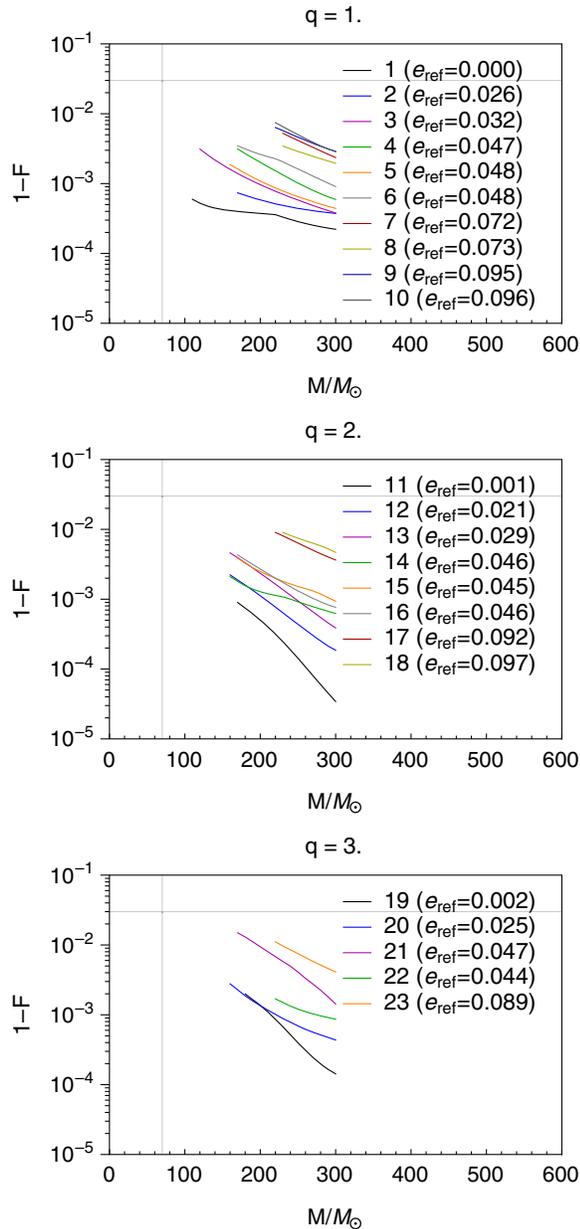
FIG. 14. The unfaithfulness, $1 - F$, for the *aLIGO design* detector configuration, between the eccentric IMR model and the NR simulations, as a function of the total binary mass. Masses for which the NR waveform starts at a frequency higher than the detector's f_{min} are omitted from the plot. The horizontal line shows the 3% unfaithfulness target, and the vertical line shows $70 M_\odot$, roughly corresponding to the mass of GW150914.

of the detector for lower mass systems) will be necessary to accurately assess the performance of the model for lower mass systems with *aLIGO design*. Improvements to the model would be needed to reach acceptable levels of faithfulness for $M \sim 70 M_\odot$ (corresponding to GW150914) for high eccentricities, with the maximum usable eccentricity being lower for *aLIGO design* than for *aLIGO O1*.

F. Comparison with quasicircular models

We now compare the eccentric IMR model with existing quasicircular ($e = 0$) models currently used by LIGO for estimating the parameters of gravitational wave sources.

Two such models are SEOBNRv4 [75] and IMRPhenomD [5,76]. These models have been compared with a large number of quasicircular NR waveforms, and the unfaithfulness is found to be <1% for *aLIGO design* in almost all cases. For *aLIGO O1*, which is less sensitive at all frequencies, the unfaithfulness will be even lower. The analogues of Fig. 14 are Fig. 2 of [75] and Fig. 15 of [5].

In the quasicircular ($e = 0$) case, the new eccentric model presented here has an unfaithfulness <1% for *aLIGO O1* for $M > 60 M_\odot$ (corresponding to the minimum mass for which we are able to compute unfaithfulness given the length of the NR waveforms), but the unfaithfulness is larger for larger eccentricities.

The quasicircular models incorporate higher order PN radiation reaction, as well as additional features designed to increase the accuracy of the dynamics, whereas the eccentric model uses simple PN for the inspiral. Further, the quasicircular models have been tested and calibrated against NR waveforms with much lower initial frequencies. As a result, we expect the low frequency behavior of the quasicircular models to be superior to the eccentric model in the quasicircular limit.

However, as we have shown, the eccentric model is faithful to the NR data for the last ~20 cycles before the merger, when the eccentricity is ≲0.1 at a time ≈7 cycles before the merger.

IX. CONCLUSIONS

We have presented 20 new publicly available nonspinning NR BBH simulations with initial eccentricities up to 0.2 and mass ratios from 1 to 3, including the merger and the preceding 20 gravitational wave cycles. When considered as sources for gravitational wave detectors, the NR waveforms start below 30 Hz for systems of total mass $M > 80 M_\odot$, and below 10 Hz for systems of total mass $M > 230 M_\odot$.

We have demonstrated that the circularization of eccentric binary black hole systems in the last few cycles before the merger first reported in [44] for equal-mass systems extends to systems with mass ratio up to $q = 3$.

We have shown that an existing PN model for the inspiral can be fitted to the NR data over one radial period shortly before the merger, and have quantified how the error in the PN model grows at earlier times. The results depend on mass ratio and eccentricity, with higher mass ratios and eccentricities generally showing a larger error at early times.

For all the NR waveforms, the PN model remains accurate to within about half a gravitational wave cycle across the entire NR waveform, but this is unlikely to be the case for longer NR waveforms.

Using the fact that the NR waveforms circularize shortly before the merger, we have shown that the merger can be represented using a circular model. A simple circular model was built from a small number of circular NR waveforms by interpolating them in the mass ratio q. A full IMR model was then constructed by blending the PN inspiral model with the NR-interpolated circular model. The combination relies on knowing the time $\Delta t(q, e, l)$ between a reference point ($x = 0.11$) in the PN waveform and the peak of the merger waveform, and we have derived an accurate empirical fitting formula for Δt from the NR waveforms.

We have compared the IMR model with all the NR simulations. For $f_{\text{low}} = 30$ Hz, and a detector configuration, *aLIGO O1*, corresponding to the first observing run of advanced LIGO, the eccentric model has a faithfulness of $\geq 97\%$ with the corresponding NR waveform for systems of total mass $M \geq 85 M_\odot$ for all the NR simulations ($e_{\text{ref}} \leq 0.1$, $q \leq 3$), and for systems of total mass $M \geq 70 M_\odot$, the faithfulness is over 97% for $e_{\text{ref}} \lesssim 0.05$ and $q \leq 3$.

The availability of eccentric IMR waveform models such as the model presented in [48], and the model presented here, which has been calibrated to and validated against NR simulations, is the first step towards measuring the eccentricity of binary black hole mergers through their gravitational wave emission. We have shown that the merger can be accurately represented by a simple combination of eccentric PN and circular NR results.

Note, however, that the present model has been validated only for the last ∼20 cycles before the merger, corresponding to the finite length of the NR simulations used. For systems of sufficiently high mass that this is the only part of the waveform which is in the sensitive band of the detector, for example sources similar to GW150914, the model may be useful for parameter estimation. For systems where longer waveforms are required, i.e., lower mass systems for which both the merger and more of the early inspiral is in the sensitive band of the detector, the model is probably not sufficiently faithful to the general relativistic waveform for reliable results to be obtained.

The model has been calibrated to NR simulations with parameters in the range ($e_{\text{ref}} \leq 0.1$, $q \leq 3$), but it can be evaluated outside its range of calibration. The model is not a small-e expansion, so in principle it may be evaluated for

any $e < 1$. However, the PN approximation, which is an expansion in v/c, will break down for high eccentricities if the velocity becomes too large at pericenter. The circular merger model, as described here, can only be reliably evaluated within its calibration range $q \leq 4$, but by including more NR simulations, an extension to higher mass ratio would be straightforward.

The simulations and model presented here are restricted to the case of nonspinning binaries. For interesting applications to gravitational wave data, the model will need to be extended to include the effects of spin, otherwise it is possible that the effects of eccentricity and spin could be confused. We also model only the dominant $\ell = 2$, $m = \pm 2$ spherical harmonic modes. While the effects of subdominant modes are likely more important for eccentric systems than for circular systems, we expect the effects to be small for the moderate eccentricities studied here. Finally, while our model is fully 3 PN accurate in the conservative dynamics, the radiation reaction terms are implemented only up to 2 PN, in contrast to the model of [48] which is 3 PN in both the conservative and radiative effects, and also contains improvements for high mass ratios based on the test-mass limit. We expect that the performance of our model during the early inspiral (when aligned just before the merger) would be improved with these modifications, but we leave that to future work.

ACKNOWLEDGMENTS

[1] B. P. Abbott *et al.* (Virgo, LIGO Scientific), Phys. Rev. Lett. **116**, 061102 (2016).

[2] B. P. Abbott *et al.* (Virgo, LIGO Scientific), Phys. Rev. Lett. **116**, 241103 (2016).

[3] B. P. Abbott *et al.* (Virgo, LIGO Scientific), Phys. Rev. Lett. **118**, 221101 (2017).

[4] A. Taracchini *et al.*, Phys. Rev. D **89**, 061502 (2014).

[5] S. Khan, S. Husa, M. Hannam, F. Ohme, M. Pürrer, X. J. Forteza, and A. Bohé, Phys. Rev. D **93**, 044007 (2016).

[6] A. H. Mroue *et al.*, Phys. Rev. Lett. **111**, 241104 (2013).

[7] B. P. Abbott *et al.* (Virgo, LIGO Scientific), Phys. Rev. Lett. **116**, 241102 (2016).

[8] P. C. Peters, Phys. Rev. 136, B1224 (1964).

[9] L. Wen, Astrophys. J. 598, 419 (2003).

[10] M. J. Benacquista and J. M. B. Downing, Living Rev. Relativity 16, 4 (2013).

[11] K. Gultekin, M. C. Miller, and D. P. Hamilton, Astrophys. J. 616, 221 (2004).

[12] O. Blaes, M. H. Lee, and A. Socrates, Astrophys. J. 578, 775 (2002).

[13] M. Dotti, M. Colpi, and F. Haardt, Mon. Not. R. Astron. Soc. 367, 103 (2006).

[14] F. Antonini, S. Chatterjee, C. L. Rodriguez, M. Morscher, B. Pattabiraman, V. Kalogera, and F. A. Rasio, Astrophys. J. 816, 65 (2016).

[15] C. L. Rodriguez, S. Chatterjee, and F. A. Rasio, Phys. Rev. D 93, 084029 (2016).

[16] K. Silsbee and S. Tremaine, Astrophys. J. 836, 39 (2017).

[17] J. Samsing, Phys. Rev. D 97, 103014 (2018).

[18] L. Gondán, B. Kocsis, P. Raffai, and Z. Frei, Astrophys. J. 860, 5 (2018).

[19] F. Antonini, S. Toonen, and A. S. Hamers, Astrophys. J. 841, 77 (2017).

[20] P. C. Peters and J. Mathews, Phys. Rev. 131, 435 (1963).

[21] R. V. Wagoner and C. M. Will, Astrophys. J. 210, 764 (1976); 215, 984(E) (1977).

[22] L. Blanchet and G. Schäfer, Mon. Not. R. Astron. Soc. 239, 845 (1989).

[23] W. Junker and G. Schäfer, Mon. Not. R. Astron. Soc. 254, 146 (1992).

[24] L. Blanchet and G. Schäfer, Classical Quantum Gravity 10, 2699 (1993).

[25] R. Rieth and G. Schäfer, Classical Quantum Gravity 14, 2357 (1997).

[26] T. Damour and G. Schäfer, Nuovo Cimento B 101, 127 (1988).

[27] G. Schäfer and N. Wex, Phys. Lett. A 174, 196 (1993).

[28] N. Wex, Classical Quantum Gravity 12, 983 (1995).

[29] T. Damour, A. Gopakumar, and B. R. Iyer, Phys. Rev. D 70, 064028 (2004).

[30] C. Königsdörffer and A. Gopakumar, Phys. Rev. D 73, 124012 (2006).

[31] R.-M. Memmesheimer, A. Gopakumar, and G. Schäfer, Phys. Rev. D 70, 104011 (2004).

[32] K. G. Arun, L. Blanchet, B. R. Iyer, and M. S. S. Qusailah, Phys. Rev. D 77, 064035 (2008).

[33] K. G. Arun, L. Blanchet, B. R. Iyer, and M. S. S. Qusailah, Phys. Rev. D 77, 064034 (2008).

[34] K. G. Arun, L. Blanchet, B. R. Iyer, and S. Sinha, Phys. Rev. D 80, 124018 (2009).

[35] N. Loutrel and N. Yunes, Classical Quantum Gravity 34, 044003 (2017).

[36] B. Moore, M. Favata, K. G. Arun, and C. K. Mishra, Phys. Rev. D 93, 124061 (2016).

[37] C. K. Mishra, K. G. Arun, and B. R. Iyer, Phys. Rev. D 91, 084040 (2015).

[38] M. Tessmer and G. Schäfer, Phys. Rev. D 89, 104055 (2014).

[39] M. Tessmer, J. Hartung, and G. Schafer, Classical Quantum Gravity 30, 015007 (2013).

[40] A. Gopakumar and G. Schafer, Phys. Rev. D 84, 124007 (2011).

[41] M. Tessmer and G. Schaefer, Ann. Phys. (Amsterdam) 523, 813 (2011).

[42] L. Blanchet, Living Rev. Relativity 17, 2 (2014).

[43] U. Sperhake, E. Berti, V. Cardoso, J. A. González, B. Brügmann, and M. Ansorg, Phys. Rev. D 78, 064069 (2008).

[44] I. Hinder, B. Vaishnav, F. Herrmann, D. Shoemaker, and P. Laguna, Phys. Rev. D 77, 081502 (2008).

[45] I. Hinder, F. Herrmann, P. Laguna, and D. Shoemaker, Phys. Rev. D 82, 024033 (2010).

[46] A. H. Mroue, H. P. Pfeiffer, L. E. Kidder, and S. A. Teukolsky, Phys. Rev. D 82, 124016 (2010).

[47] C. O. Lousto, J. Healy, and H. Nakano, Phys. Rev. D 93, 044031 (2016).

[48] E. A. Huerta et al., Phys. Rev. D 95, 024038 (2017).

[49] B. J. Kelly, J. G. Baker, W. D. Boggs, S. T. McWilliams, and J. Centrella, Phys. Rev. D 84, 084009 (2011).

[50] T. Hinderer and S. Babak, Phys. Rev. D 96, 104048 (2017).

[51] Z. Cao and W.-B. Han, Phys. Rev. D 96, 044028 (2017).

[52] E. A. Huerta et al., Phys. Rev. D 97, 024031 (2018).

[53] https://www.black-holes.org/waveforms/catalog.php.

[54] https://github.com/ianhinder/EccentricIMR.

[55] A. Gopakumar and B. R. Iyer, Phys. Rev. D 56, 7708 (1997).

[56] A. Gopakumar and B. R. Iyer, Phys. Rev. D 65, 084011 (2002).

[57] E. Poisson and C. Will, Gravity: Newtonian, Post-Newtonian, Relativistic (Cambridge University Press, Cambridge, England, 2014).

[58] M. Boyle, D. Brown, L. Kidder, A. Mroué, H. Pfeiffer, M. Scheel, G. Cook, and S. Teukolsky, Phys. Rev. D 76, 124038 (2007).

[59] I. MacDonald, A. H. Mroue, H. P. Pfeiffer, M. Boyle, L. E. Kidder, M. A. Scheel, B. Szilagyi, and N. W. Taylor, Phys. Rev. D 87, 024009 (2013).

[60] http://www.black-holes.org/SpEC.html.

[61] M. A. Scheel, H. P. Pfeiffer, L. Lindblom, L. E. Kidder, O. Rinne, and S. A. Teukolsky, Phys. Rev. D 74, 104006 (2006).

[62] B. Szilagyi, L. Lindblom, and M. A. Scheel, Phys. Rev. D 80, 124010 (2009).

[63] L. T. Buchman, H. P. Pfeiffer, M. A. Scheel, and B. Szilagyi, Phys. Rev. D 86, 084033 (2012).

[64] L. Lindblom, M. A. Scheel, L. E. Kidder, R. Owen, and O. Rinne, Classical Quantum Gravity 23, S447 (2006).

[65] H. Friedrich, Commun. Math. Phys. 100, 525 (1985).

[66] F. Pretorius, Phys. Rev. Lett. 95, 121101 (2005).

[67] L. Lindblom and B. Szilagyi, Phys. Rev. D 80, 084019 (2009).

[68] D. A. Hemberger, M. A. Scheel, L. E. Kidder, B. Szilágyi, G. Lovelace, N. W. Taylor, and S. A. Teukolsky, Classical Quantum Gravity 30, 115001 (2013).

[69] M. A. Scheel, M. Giesler, D. A. Hemberger, G. Lovelace, K. Kuper, M. Boyle, B. Szilágyi, and L. E. Kidder, Classical Quantum Gravity 32, 105009 (2015).

[70] H. P. Pfeiffer, D. A. Brown, L. E. Kidder, L. Lindblom, G. Lovelace, and M. A. Scheel, New frontiers in numerical relativity, in Proceedings of the International Meeting,

NFNR 2006, Potsdam, Germany, 2006 [*Classical Quantum Gravity* 24, S59 (2007)].

[71] B. Szilágyi, Int. J. Mod. Phys. D **23**, 1430014 (2014).

[72] M. Boyle and A. H. Mroue, Phys. Rev. D **80**, 124045 (2009).

[73] I. Hinder *et al.*, Classical Quantum Gravity **31**, 025012 (2014).

[74] J. Healy, C. O. Lousto, H. Nakano, and Y. Zlochower, Classical Quantum Gravity **34**, 145011 (2017).

[75] A. Bohé *et al.*, Phys. Rev. D **95**, 044028 (2017).

[76] S. Husa, S. Khan, M. Hannam, M. Pürrer, F. Ohme, X. J. Forteza, and A. Bohé, Phys. Rev. D **93**, 044006 (2016).

[77] J. Blackman, S. E. Field, C. R. Galley, B. Szilágyi, M. A. Scheel, M. Tiglio, and D. A. Hemberger, Phys. Rev. Lett. **115**, 121102 (2015).

[78] S. A. Usman *et al.*, Classical Quantum Gravity **33**, 215004 (2016).

[79] C. Messick *et al.*, Phys. Rev. D **95**, 042001 (2017).

[80] J. Veitch *et al.*, Phys. Rev. D **91**, 042003 (2015).

[81] L. S. Finn, Phys. Rev. D **46**, 5236 (1992).

[82] https://github.com/ligo-cbc/pycbc-config/blob/master/O1/psd/H1L1-ER8_HARM_MEAN_PSD-1126033217-223200.txt.gz.

[83] D. Shoemaker (LIGO Collaboration), Advanced LIGO anticipated sensitivity curves, LIGO Document No. T0900288-v3, 2010.

[84] T. Damour, B. R. Iyer, and B. S. Sathyaprakash, Phys. Rev. D **57**, 885 (1998).

[85] E. W. Hansen, *Fourier Transforms: Principles and Applications* (Wiley, New York, 2014).

[86] D. J. A. McKechan, C. Robinson, and B. S. Sathyaprakash, Gravitational waves, in *Proceedings of the 8th Edoardo Amaldi Conference, Amaldi 8, New York, 2009* [*Classical Quantum Gravity* 27, 084020 (2010)].

[87] S. Droz, D. J. Knapp, E. Poisson, and B. J. Owen, Phys. Rev. D **59**, 124016 (1999).

[88] T. Damour, B. R. Iyer, and B. S. Sathyaprakash, Phys. Rev. D **62**, 084036 (2000).

[89] A. Taracchini (private communication).

[90] I. Hinder and B. Wardell, SIMULATIONTOOLS for Mathematica, http://simulationtools.org.